

Three-dimensional variations of atmospheric CO₂: aircraft measurements and multi-transport model simulations

Y. Niwa¹, P. K. Patra², Y. Sawa¹, T. Machida³, H. Matsueda¹, D. Belikov³, T. Maki¹, M. Ikegami⁴, R. Imasu⁵,
S. Maksyutov³, T. Oda^{3,*,**}, M. Satoh^{5,2}, and M. Takigawa²

¹Geochemical Research Department, Meteorological Research Institute, 1-1 Nagamine, Tsukuba, Ibaraki, 305-0052, Japan

²Research Institute for Global Change/JAMSTEC, 3173-25 Showa-machi, Yokohama, Kanagawa, 236-0001, Japan

³Center for Global Environmental Research, National Institute for Environmental Studies, 16-2 Onogawa, Tsukuba, Ibaraki, 305-8506, Japan

⁴Japan Meteorological Agency, 1-3-4 Otemachi, Chiyoda-ku, Tokyo, 100-8122, Japan

⁵Atmosphere and Ocean Research Institute, The University of Tokyo, 5-1-5 Kashiwanoha, Kashiwa, Chiba, 277-8568, Japan

* now at: Cooperative Institute for Research in the Atmosphere, Colorado State University, Fort Collins, CO 80523-1375, USA

** now at: National Oceanic and Atmospheric Administration, Earth System Research Laboratory, Boulder, CO 80305, USA

Received: 8 April 2011 – Published in Atmos. Chem. Phys. Discuss.: 27 April 2011

Revised: 23 September 2011 – Accepted: 17 December 2011 – Published: 22 December 2011

Abstract. Numerical simulation and validation of three-dimensional structure of atmospheric carbon dioxide (CO₂) is necessary for quantification of transport model uncertainty and its role on surface flux estimation by inverse modeling. Simulations of atmospheric CO₂ were performed using four transport models and two sets of surface fluxes compared with an aircraft measurement dataset of Comprehensive Observation Network for Trace gases by Air-Liner (CONTRAIL), covering various latitudes, longitudes, and heights. Under this transport model intercomparison project, spatiotemporal variations of CO₂ concentration for 2006–2007 were analyzed with a three-dimensional perspective. Results show that the models reasonably simulated vertical profiles and seasonal variations not only over northern latitude areas but also over the tropics and southern latitudes. From CONTRAIL measurements and model simulations, intrusion of northern CO₂ in to the Southern Hemisphere, through the upper troposphere, was confirmed. Furthermore, models well simulated the vertical propagation of seasonal variation in the northern free troposphere. However, significant model-observation discrepancies were found in Asian regions, which are attributable to uncertainty of the surface CO₂ flux data. In summer season, differences in latitudinal gradients by the fluxes are comparable to or greater

than model-model differences even in the free troposphere. This result suggests that active summer vertical transport sufficiently ventilates flux signals up to the free troposphere and the models could use those for inferring surface CO₂ fluxes.

1 Introduction

Better understanding of the global and regional carbon budget would support more reliable prediction of future climate with an earth system model. However, the accuracy of source/sink estimation of carbon dioxide (CO₂) by inverse modeling, which is a leading method to estimate regional carbon budgets, is not sufficiently high because of the errors in forward model transport and sparse observation coverage. In fact, inverted CO₂ fluxes are affected strongly by transport model properties. The TransCom3 models showed large differences of the so-called rectifier effect (Denning et al., 1996). In inversions, a larger rectifier effect produces stronger uptake in northern terrestrial areas, thereby compensating stronger sources in tropical terrestrial areas, and vice versa. On average they estimated a strong northern terrestrial sink of 2.4 Pg C yr⁻¹ and strong tropical terrestrial source of 1.8 Pg C yr⁻¹ for the time period of 1992–1996 (Gurney et al., 2004). However, this source/sink distribution has not been fully validated because of insufficient observational data for the tropics and because of large model uncertainties.



Correspondence to: Y. Niwa
(yniwa@mri-jma.go.jp)

Later, using measurements of CO₂ obtained using aircraft at 12 sites, Stephens et al. (2007) showed the utility of vertical profiles in validating atmospheric inversions. By investigating vertical CO₂ gradients and selecting 3 out of 12 TransCom3 inversions, they inferred -1.5 and 0.1 Pg C yr⁻¹ respectively for the northern and tropical terrestrial carbon budgets for the same period of TransCom3. However, Stephens et al. (2007) suggested that most of the transport models were biased to ventilate too much of CO₂ uptake signal from the planetary boundary layer (PBL) to the free troposphere (FT) during boreal summer. Moreover, the recent validation of CO₂ inversions by Pickett-Heaps et al. (2011) showed inconsistencies between inversions and independent vertical profiles.

Therefore, verifying the quality of the vertical CO₂ transport by model is urgently required. Simultaneously, modelled horizontal gradient of CO₂ in the upper-troposphere should be also verified. However, our understanding of global-scale CO₂ distributions in the FT remained limited. The aircraft measurement sites used in the previous studies were located mainly in mid-latitude to high latitude areas in the Northern Hemisphere. Especially, aircraft measurement networks have not fully covered the Asian areas such as southern and Southeast Asia. Meanwhile, regional features of upper-air CO₂ have been surveyed over Europe and North America through aircraft campaigns (Gerbig et al., 2003; Sarrat et al., 2007; Crevoisier et al., 2010; Xueref-Remy et al., 2011).

In this study, we analyzed CO₂ model simulation results extensively using vertical profiles of CO₂, which are located throughout the globe, and surface measurements. The vertical profile measurements were taken from an aircraft CO₂ measurement project: Comprehensive Observation Network for Trace gases by Airliner (CONTRAIL) (Machida et al., 2008; Matsueda et al., 2008; Sawa et al., 2008). The surface measurements were taken from GLOBALVIEW-CO₂ (2010). The CONTRAIL project measures atmospheric CO₂ concentrations covering altitudes between the earth's surface to the upper-troposphere/lower-stratosphere (UT/LS), and covering latitudes between the boreal high latitudes to the austral mid-latitudes including many parts of Asia. Although the vertical profiles from CONTRAIL are being used for validating inverse modelled fluxes (e.g., Chevallier et al., 2010), a detailed vertical profile comparison covering different geographical regions has not been conducted.

Therefore, the first aim of our study is to elucidate detailed structures of the atmospheric CO₂ in a three-dimensional view and to investigate model performances in reproducing those variations. The second aim is to draw some inferences to improve the precision of regional carbon budgets using the CONTRAIL measurements; such wide-ranging aircraft data have never been used in inversion studies before. As a multi-model framework provides more robust results and improves the inference of the range of model uncertainty (Geels et al., 2007; Law et al., 2008; Patra et al., 2008), we used four in-

dependent forward transport models that were developed or updated recently. Furthermore, we used two datasets of surface CO₂ flux to evaluate the relative contributions of one possible flux uncertainty to three-dimensional CO₂ concentration fields. We first describe the flux datasets, the transport models, and the observations as well as the simulation settings in Sect. 2. In the subsequent Sect. 3, we first introduce transport features of each model using simulation results of sulfur hexafluoride (SF₆) and radon (²²²Rn). Subsequently, we show vertical profiles, seasonal variations and latitudinal profiles of the simulated and observed CO₂. Concluding remarks are presented in Sect. 4.

2 Experimental settings

The transport models were run using analyzed meteorology and prescribed surface fluxes during 2001–2007. The first five years (2001–2005) of the simulation were used as the model spin-up; the later period (2006–2007) was used for analysis in comparison with surface and aircraft observations. In addition to the CO₂ simulations, we simulated SF₆ and radon to investigate the overall model transport properties. All the initial concentrations were set to zero/constant everywhere.

2.1 Surface fluxes

The first set of CO₂ flux (Flux1) is prepared by combining seasonally varying fluxes of terrestrial biosphere photosynthesis/respiration from the Carnegie-Ames-Stanford Approach (CASA) model (Randerson et al., 1997), and of oceanic exchange based on CO₂ partial pressure measurements by oceanographic research vessels (Takahashi et al., 2009), and fossil fuel emissions with annual trends are further added. Fossil fuel emissions are derived from EDGAR-1998 distribution (Olivier and Berdowski, 2001) and the emission totals are scaled using the growth rate of top 20 country-specific fossil fuel consumptions from CDIAC (Boden et al., 2009). To consider a diurnal cycle of CO₂ flux from terrestrial ecosystems, the monthly means of CASA flux are distributed onto three-hourly time steps using 2 m air temperature and downward shortwave radiation data of Japanese 25-yr ReAnalysis/JMA Climate Data Assimilation System (JRA-25/JCDAS) (Onogi et al., 2007) using the method described by Olsen and Randerson (2004). This experimental protocol resembles that of the TransCom continuous experiment (Law et al., 2008), except that we use inter-annually varying fossil CO₂ flux.

The second set (Flux2) is inversion flux combined with identical fossil fuel emissions as in Flux1. The inversion flux represents all non-fossil source/sink distribution over land and ocean, derived by inverse modeling with 12 TransCom3 models (Gurney et al., 2004) and observational data from GLOBALVIEW-CO₂ at 87 sites during 1999–2001 (ref.

Table 1. Regionally aggregated non-fossil fuel carbon budgets (unit is Pg C yr⁻¹) of Flux1 and Flux2. Definition of the regional boundary is the same as that of TransCom3 (Gurney et al., 2004).

Region Name	JFM		JAS		Annual total	
	Flux1	Flux2	Flux1	Flux2	Flux1	Flux2
Northern Land	7.44	5.95	-11.26	-12.70	0.00	-1.38
Tropical Land	4.74	6.25	-3.90	-2.82	0.00	1.35
Southern Land	-3.98	-4.62	5.16	5.22	0.00	-0.72
Northern Ocean	-1.59	-2.44	-0.11	-1.45	-1.00	-1.67
Tropical Ocean	0.67	0.62	0.79	0.88	0.70	0.94
Southern Ocean	-0.95	-1.51	-1.21	-1.53	-1.11	-1.32

Table 2. List of the transport models, and their fundamental characteristics.

Model name	Cumulus convection	Vertical turbulent mixing	Winds	SF ₆ gradient at 400/850 hPa*	Vertical ²²² Rn gradient for JAS**	Vertical CO ₂ gradient in NH for JAS***
ACTM	Arakawa-Schubert	Mellor-Yamada 2	NCEP2	0.16/0.25	5.83	-0.70
MJ98-CDTM	Kuo and Tiedtke	Mellor-Yamada 2	JCDAS	0.11/0.21	13.06	-1.66
NICAM-TM	Arakawa-Schubert	Mellor-Yamada 2 and Nakanishi-Niino	JCDAS	0.14/0.23	5.23	-0.38
NIES	Grell	ECMWF PBL height	JCDAS	0.18/0.26	8.01	-0.80

* SF₆ gradient is defined as the difference between the annual mean concentrations of the two-hemispheres.

** Vertical radon gradient is defined as the difference of the global July-August-September (JAS) mean concentrations between at 300 and 850 hPa.

*** Vertical CO₂ gradient is defined as the difference of JAS mean concentrations between at 850 hPa and 500 hPa in the Northern Hemisphere.

Miyazaki et al. (2008) for an overall description). This inversion flux is derived as an average of 1999–2001, when no strong El Niño or La Niña was experienced. Therefore, Flux2 can be considered as a near climatological inversion flux.

The global total net fluxes for 2007 are, respectively, 7.0 Pg C yr⁻¹ and 5.6 Pg C yr⁻¹, corresponding to Flux1 and Flux2. The non-fossil fuel fluxes of Flux1 and Flux2 are used repeatedly for different years. The annual and seasonal net non-fossil fuel fluxes for each latitudinal area are summarized in Table 1.

The SF₆ emission distribution is taken from the EDGAR-1998 with the yearly emission change scaled to the global SF₆ growth rate estimated from measurements by Earth System Research Laboratory/National Oceanic and Atmospheric Administration (ESRL/NOAA). Radon emission data are referred from Jacob et al. (1997).

2.2 Transport models

We used three on-line models and one off-line model for the simulations (Table 2). An on-line model calculates tracer transport within an atmospheric general circulation model (AGCM), in which meteorological fields are fully calculated and are nudged towards the analyzed fields using Newtonian relaxation methods (nudging). Meanwhile, in an off-

line model, only tracer transport is calculated using already prepared meteorological fields from the analyzed data. Three of the four transport models are nudged with the same JRA-25/JCDAS horizontal winds. However, the choice of meteorological reanalysis product has less influence on the quality of model simulations as seen in the TransCom continuous experiment (Law et al., 2008; Patra et al., 2008), which also demonstrated sizeable differences between models driven by same reanalysis. Three-dimensional tracer distributions are largely influenced by sub-grid scale parameterized vertical transport of turbulent mixing and cumulus convection.

2.2.1 ACTM

The on-line chemical transport model ACTM is based on the Center for Climate System Research/National Institute for Environmental Studies/Frontier Research Center for Global Change (CCSR/NIES/FRCGC) AGCM. Cumulus convections are parameterized by the scheme of Arakawa and Schubert (1974). For vertical turbulent mixing, level 2 scheme of Mellor and Yamada (1974) is used. In the ACTM simulations, the horizontal resolution of T42 spectral truncations (approximately 2.8° × 2.8°) is used. The number of the vertical layers is 32. For nudging, the ACTM uses six-hourly horizontal velocities and temperature from the National Center for Environmental Prediction/DOE AMIP-II Reanalysis

(NCEP2; Kanamitsu et al., 2002). Further information of ACTM is available in Takigawa et al. (2005) and Patra et al. (2009).

2.2.2 MJ98-CDTM

The on-line model MJ98-CDTM was developed at the Japan Meteorological Agency (JMA) and the Meteorological Research Institute (MRI) (Shibata et al., 1999; Maki et al., 2009). The horizontal resolution of MJ98-CDTM is also T42; the number of vertical layers is 30. The vertical turbulent scheme is level 2 of Mellor and Yamada (1974). The Kuo (1974) scheme is used for deep cumulus convection and Tiedtke (1989) is used for shallow convection. The model uses the six-hourly horizontal wind velocities from JRA-25/JCDAS for nudging.

2.2.3 NICAM-TM

The Nonhydrostatic ICosahedral Atmospheric Model (NICAM; Tomita and Satoh, 2004; Satoh et al., 2008)-based transport model (NICAM-TM) was developed by Niwa (2010). The NICAM is a quasi-homogeneous grid AGCM: the horizontal grids are generated by dividing an icosahedron recursively. The tracer advection scheme preserves both monotonicity and consistency with continuity using a monotonic scheme of Miura (2007) (Niwa et al., 2011). The vertical turbulent scheme is MYNN Level 2 (Mellor and Yamada, 1974; Nakanishi and Niino, 2004; Noda et al., 2009). Cumulus convections are parameterized using the scheme of Arakawa and Schubert (1974). The NICAM simulations were performed using horizontal resolution of glevel-5 (5 is the number of divisions of an icosahedron to construct the horizontal grid; the grid interval is about 240 km). The number of vertical layers is 40 and the top of the model domain is about 45 km. The six-hourly horizontal wind velocities from JRA-25/JCDAS are used for nudging.

2.2.4 NIES

The National Institute for Environmental Studies (NIES) global transport model, with its flux-form advection algorithm (Belikov et al., 2011), is implemented on hybrid isentropic (σ - θ) vertical coordinate systems (model version denoted as NIES-08.1i.). The model is off-line and driven by JRA-25/JCDAS. Kuo-type penetrative cloud convection scheme is based on Grell (1993) including entrainment and detrainment processes on convective updrafts and downdrafts, as proposed by Tiedtke (1989). Cumulus convective updraft rate are calculated using the convective precipitation rate by JCDAS reanalysis, contrary to using large-scale moisture divergence used in Tiedtke (1989). The spatial resolution was set to $2.5^\circ \times 2.5^\circ$ in the horizontal direction. The vertical coordinate contains 32 levels, with the isentropic part starting at 350 K. The three-hourly PBL height is taken from the ECMWF Interim Reanalysis (Simmons et al., 2007).

2.3 Aircraft and surface station measurements of CO₂

In the CONTRAIL project, measurement instruments are installed in commercial airliners. We used high-frequency data on Japan Airlines (JAL) flight paths obtained by five on-board continuous CO₂ measuring equipments (CMEs; Machida et al., 2008) during 2006–2007. From comparison with occasional flask sampling using automatic sampling equipment (ASE), the accuracy of the data is assured within 0.2 ppm (Matsueda et al., 2008). During 2006–2007, CONTRAIL measurement flights were conducted over East Asia (EAS), Europe (EUR), western North America (WNA), Hawaii (HWI), the Indian subcontinent (IND), northern and southern Southeast Asia (NSA, SSA), southern North America (SNA) and Australia (AUS) (Fig. 1 and Table 3). The measurement data were averaged for 1 min, corresponding to about 10–15 km horizontal distance at cruising altitude and 10 s corresponding to about 50–200 m vertical distance during ascent or descent near the airports. The measurement locations were corrected in advance according to the measurement lag time. The horizontal distance travelled during the profiles from ascents and descents is about 200–400 km.

Surface CO₂ time series are taken from GLOBALVIEW-CO₂, a data product prepared using measurements from multiple institutions, following the methodology of Masarie and Tans (1995). To ascertain background features of surface CO₂, we chose 10 sites in marine boundary layer (MBL) from the dataset. The locations of those sites are portrayed in Fig. 1 and are also presented in Table 4.

2.4 Data processing for CO₂

The simulated atmospheric CO₂ data for 2006–2007 were extracted at the same time and locations as those of the CONTRAIL measurements by linear interpolation to the measurement space–time coordinates. In CONTRAIL measurements, altitude data are recorded as the pressure altitude. The model data were interpolated vertically using pressure data.

For the analysis, we used the detrended seasonal cycle of CO₂ (Δ CO₂) with reference to a linear trend at a background site because the simulated CO₂ growth rate is not optimized for the observed growth rate for 2006–2007. The simulated and observed data were respectively subtracted using a linear trend function derived from each CO₂ record at Minamitorishima (24.30° N, 153.97° E), which is a remote marine site in the western North Pacific. First, the CO₂ record at Minamitorishima was fitted with a function combining linear trend with harmonics as

$$\text{CO}_2(t) = a_0 + a_1 t + \sum_{n=1}^2 [a_{2n} \sin(2n\pi t) + a_{2n+1} \cos(2n\pi t)], \quad (1)$$

where t is time (calendar year) and a_i ($i = 0, 1, \dots, 5$) is a parameter optimized using least-squares method. Then the

Table 3. List of airports for the CONTRAIL CO₂ measurement, and number of flights at each airport. Latitudes and longitudes are calculated by averaging those of the measurement points during take-offs and landings.

City	Code	Latitude	Longitude	Number of Flights		Region
				2006	2007	
Narita	NRT	35.60° N	140.36° E	411	1044	EAS
Osaka	KIX	34.54° N	135.15° E	60	205	EAS
Nagoya	NGO	35.22° N	136.89° E	74	172	EAS
Paris	CDG	49.92° N	3.41° E	52	107	EUR
Vancouver	YVR	49.10° N	123.91° W	44	115	WNA
Jakarta	CGK	5.42° S	107.26° E	41	106	SSA
Fukuoka	FUK	33.81° N	131.01° E	30	102	EAS
London	LHR	51.86° N	1.26° E	23	108	EUR
Incheon	ICN	37.15° N	127.51° E	32	72	EAS
Honolulu	HNL	21.55° N	158.92° W	27	75	HWI
Taipei	TPE	25.49° N	121.92° E	5	90	EAS
Bangkok	BKK	14.17° N	101.52° E	17	70	NSA
Delhi	DEL	28.20° N	77.95° E	18	66	IND
Singapore	SIN	1.89° N	104.42° E	34	47	SSA
Tokyo	HND	35.13° N	139.64° E	6	56	EAS
Pusan	PUS	35.16° N	129.83° E	33	22	EAS
Milan	MLX	46.09° N	9.46° E	28	20	EUR
Denpasar	DPS	8.01° S	115.36° E	2	44	SSA
Mexico City	MEX	19.92° N	99.48° W	9	32	SNA
Roma	FCO	42.76° N	12.48° E	16	24	EUR
Amsterdam	AMS	52.94° N	6.10° E	0	40	EUR
Sydney	SYD	33.14° S	150.88° E	13	26	AUS
Osaka	ITM	34.63° N	136.06° E	0	32	EAS
Moscow	SVO	56.87° N	37.88° E	8	18	EUR
Brisbane	BNE	26.54° S	152.64° E	0	22	AUS
Los Angeles	LAX	34.42° N	119.03° W	18	0	WNA
Chitose	CTS	42.06° N	141.62° E	2	8	EAS
Ulaanbaatar	ULN	47.46° N	107.31° E	4	2	EAS
Guam	GUM	14.27° N	144.56° E	4	2	NSA
Zurich	ZRH	48.55° N	8.95° E	4	0	EUR
Naha	OKA	26.46° N	128.04° E	2	2	EAS
Hiroshima	HIJ	34.79° N	133.76° E	0	4	EAS
Kuala Lumpur	KUL	2.82° N	102.62° E	2	0	SSA
Alice Springs	ASP	23.76° S	134.41° E	2	0	AUS
Las Vegas	LAS	36.45° N	116.06° W	2	0	WNA
Manila	MNL	14.78° N	121.60° E	0	2	NSA
Budapest	BUD	48.51° N	19.68° E	0	2	EUR
Iwakuni	IWJ	33.81° N	133.02° E	0	2	EAS
Sendai	SDJ	38.04° N	141.61° E	0	2	EAS

ΔCO_2 value at an arbitrary place x and time t was calculated as

$$\Delta\text{CO}_2(x, t) = \text{CO}_2(x, t) - a_0 - a_1 t. \quad (2)$$

Furthermore, the ΔCO_2 data were averaged into bins before analysis to avoid excessive weights of specific regions where measurements are conducted frequently (e.g. Japan). Bins are defined horizontally in each $10^\circ \times 10^\circ$ latitude-longitude grid, vertically at each level with 1 km height, and temporally for each month.

3 Results and discussion

3.1 General features of the transport models

Figure 2 shows the latitudinal gradient of annual zonal mean of SF₆ concentrations at 400 hPa and 850 hPa. At both levels, MJ98-CDTM has the smallest north-south gradient (0.11, 0.21 ppt for 400 hPa and 850 hPa), whereas NIES has the largest one (0.18, 0.26 ppt for 400 hPa and 850 hPa). Because the emissions of SF₆ occur over more densely populated areas in the Northern Hemisphere than in the

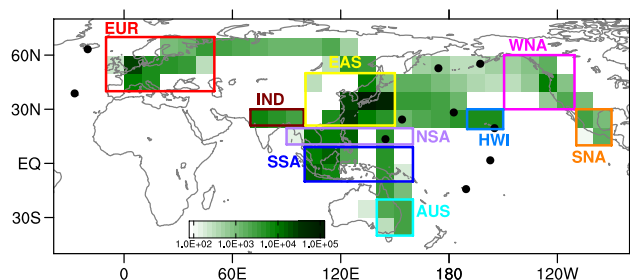


Fig. 1. Number of data in each latitude-longitude grid ($10^\circ \times 10^\circ$) (green shaded) and area distinctions used for the analyses in this study: Europe (EUR: $40\text{--}70^\circ\text{N}$, $10^\circ\text{W--}50^\circ\text{E}$), western North America (WNA: $30\text{--}60^\circ\text{N}$, $110\text{--}150^\circ\text{W}$), East Asia (EAS: $20\text{--}50^\circ\text{N}$, $100\text{--}150^\circ\text{E}$), Hawaii (HWI: $20\text{--}30^\circ\text{N}$, $150\text{--}170^\circ\text{W}$), southern North America (SNA: $10\text{--}30^\circ\text{N}$, $90\text{--}110^\circ\text{W}$), Indian continent (IND: $20\text{--}30^\circ\text{N}$, $70\text{--}100^\circ\text{E}$), northern Southeast Asia (NSA: $10\text{--}20^\circ\text{N}$, $90\text{--}160^\circ\text{E}$), southern Southeast Asia (SSA: $10^\circ\text{S--}10^\circ\text{N}$, $100\text{--}160^\circ\text{E}$) and Australia (AUS: $20\text{--}40^\circ\text{S}$, $140\text{--}160^\circ\text{E}$). Details of airport locations are presented in Table 3. Solid black circles denote locations of the selected GLOBALVIEW-CO₂ marine boundary layer sites.

Table 4. Selected surface marine boundary layer sites of GLOBALVIEW-CO₂ network.

Site name	Latitude	Longitude	Code
Storhofdi, Vestmannaeyjar	63.40°N	20.29°W	ice_01D0
Cold Bay, Alaska	55.21°N	162.72°W	cba_01D0
Shemya Island, Alaska	52.72°N	174.10°E	shm_01D0
Terceira Island, Azores	38.77°N	27.38°W	azr_01D0
Sand Island, Midway	28.21°N	177.38°W	mid_01D0
Minamitorishima	24.30°N	153.97°E	mnm_19C0
Cape Kumukahi, Hawaii	19.52°N	154.82°W	kum_01D0
Mariana Islands, Guam	13.43°N	144.78°E	gmi_01D0
Christmas Island	1.70°N	157.17°W	chr_01D0
Tutuila, American Samoa	14.25°S	170.56°W	smo_01C0

Southern Hemisphere, a smaller SF₆ gradient between the northern and Southern Hemispheres indicates a faster inter-hemispheric exchange rate. Therefore, from Fig. 2, we infer that MJ98-CDTM has the fastest inter-hemispheric exchange rate and NIES has the slowest one. Within the range of the former two, the exchange rate of ACTM is on the slower side and that of NICAM-TM is on the faster side.

Figure 3 shows the horizontal distribution of the simulated radon concentrations at 850 hPa, 500 hPa and 300 hPa for July–August–September (JAS). Results showed that MJ98-CDTM simulates much lower radon concentrations than the other three models (global averages of the radon mole fractions are 4.78 , 1.64 , 3.96 , and 4.64×10^{-21} , respectively for ACTM, MJ98-CDTM, NICAM-TM, and NIES). Radon is a short-lived tracer. Therefore, the low radon concentration suggests that vertical transport of MJ98-CDTM is slower

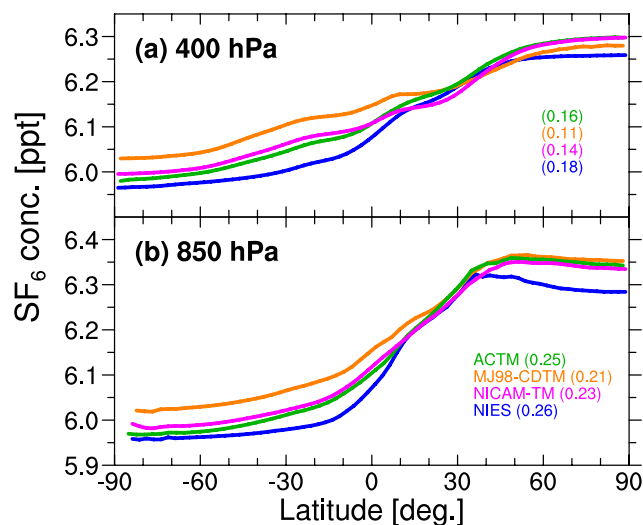


Fig. 2. Latitudinal distributions of annual zonal mean of SF₆ concentrations at 400 hPa (a) and 850 hPa (b), simulated by ACTM (green), MJ98-CDTM (orange), NICAM-TM (magenta), and NIES (blue). Parenthetical values represent differences of area-weighted mean SF₆ concentrations between in the Northern and Southern Hemispheres. The global constant offset of 4.7 ppt is added to the simulation results according to the estimate by ESRL/NOAA for the global average at the beginning of the simulation.

than those of the other models. At 500 hPa, however, the simulated radon concentrations are comparable with each other, although the ranking of the global average is the same as that at 300 hPa. The global averages of the radon mole fraction at 500 hPa are in the smaller range of $3.26\text{--}4.27 \times 10^{-21}$. Consequently, compared to the mid-troposphere, the radon concentration in the upper troposphere is quite sensitive to vertical transport, which is likely to be predominated by deep cumulus convection. At 850 hPa, NICAM-TM and ACTM (uses Arakawa-Schubert type cumulus convection schemes) show relatively low concentration compared to those of MJ98-CDTM and NIES (uses Kuo type scheme). These differences suggest the transport model properties are diverse and suitable for transport model inter-comparison experiment. Compared to earlier studies (Mahowald et al., 1997; Jacob et al., 1997; Dentener et al., 1999), the June–July–August radon concentration at 300 hPa in the upper troposphere simulated by ACTM, NICAM-TM, and NIES are somewhat on the larger side and that by MJ98-CDTM is on the smaller side (not shown).

Figure 4 shows seasonal mean vertical differences of simulated atmospheric CO₂ between 850 hPa and 500 hPa for January–February–March (JFM) and July–August–September (JAS) calculated from Flux2. For JAS, both MJ98-CDTM and NIES simulated larger CO₂ vertical differences over northern land, although ACTM and NICAM-TM simulated smaller ones. For JFM, MJ98-CDTM simulated smaller vertical differences over northern lands than the other models

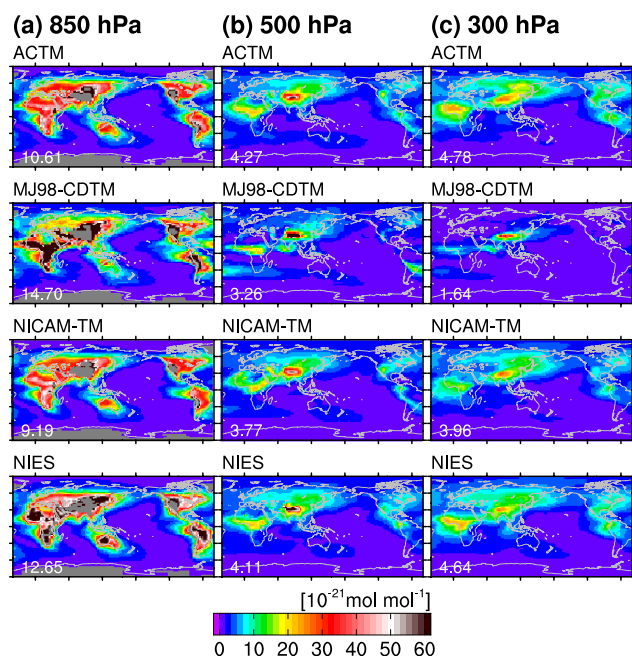


Fig. 3. Longitude–latitude distributions of radon concentrations at 850 hPa (a), 500 hPa (b) and 300 hPa (c) for July–August–September (JAS) of 2007 simulated by the models: ACTM (uppermost panels), MJ98-CDTM (middle upper panels), NICAM-TM (middle lower panels), and NIES (lowest panels). Values at the lower left corner in panels are the global average of radon mole fraction [10^{-21} mol mol⁻¹].

did. Probably it is because the shallow convection scheme of Tiedtke (1989) only used in MJ98-CDTM tends to mix concentrations at lower altitudes more strongly. There are also other possible reasons to contribute to the difference such as boundary layer scheme and difference in wind data which is treated differently in offline and online models. NIES model uses mass flux correction, while MJ98-CDTM does not. Consequently, both ACTM and NICAM-TM have weaker vertical mixing between 850 hPa and 500 hPa for boreal winter and stronger one for boreal summer. In contrast, MJ98-CDTM has a stronger one for boreal winter and a weaker one for boreal summer. In the case of NIES, it is on the weaker side for both boreal winter and summer.

3.2 Vertical profiles over the airports

Figure 5 presents seasonally varying vertical profiles of the CONTRAIL CO₂ measurements and the model simulations over each area, the spatial coverage of which is presented in Fig. 1. Figure 5 also presents time–altitude cross-sections of the observed daily Δ CO₂ for 2006 and 2007, showing that much more data were obtained for 2007 than for 2006 in most areas. As the figure shows, the models reasonably reproduced the observed vertical profiles; average correlation coefficients are 0.83 and 0.85 (significant at 95 % confidence

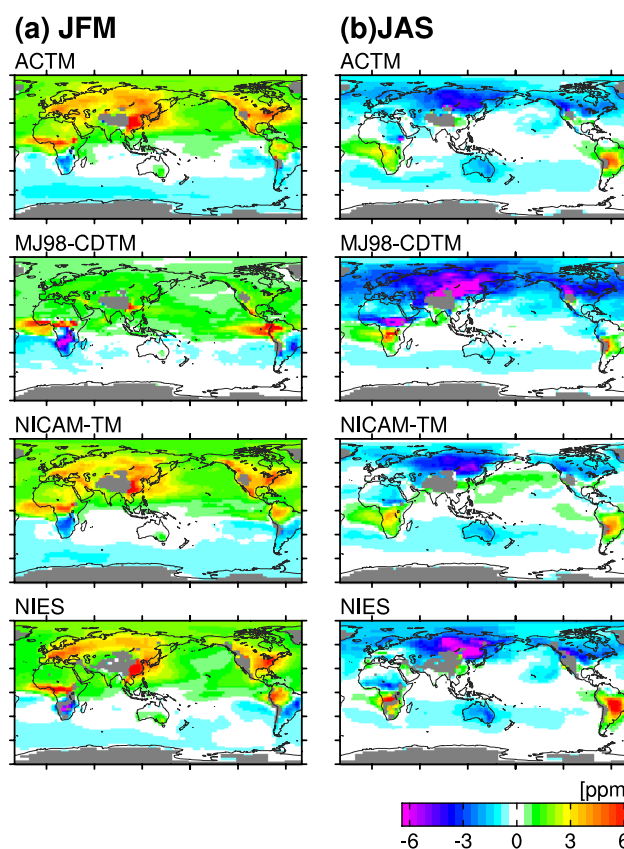


Fig. 4. Seasonal mean vertical difference of CO₂ between 850 hPa and 500 hPa for JFM (a) and JAS (b) of 2007, simulated by ACTM (uppermost panels), MJ98-CDTM (middle upper panels), NICAM-TM (middle lower panels), and NIES (lowest panels) using Flux2. Positive values mean that the CO₂ concentration at 850 hPa is larger than that at 500 hPa.

level), respectively, for the results obtained using Flux1 and Flux2. Hereafter, we use average correlation coefficients to check the compatibility between the models and the observation. Correlation coefficients are transformed into Fisher's z prior to averaging and the average coefficient is derived by back transforming the averaged z . Here, the average correlations are from 144 model–observation correlations (4 models \times 4 seasons \times 9 regions). Although general transport features are similar in ACTM and NICAM-TM as shown in Fig. 2 and 3, the differences of the vertical profiles between the two models are comparable to those between other models in some locations (e.g. IND). It suggests that vertical profiles are sensitive to local/regional transport process. The differences at IND may arise from the different wind fields (ACTM uses NCEP2 and NICAM-TM uses JCDAS for the nudging data) or the different Mellor–Yamada type scheme for vertical turbulent mixing.

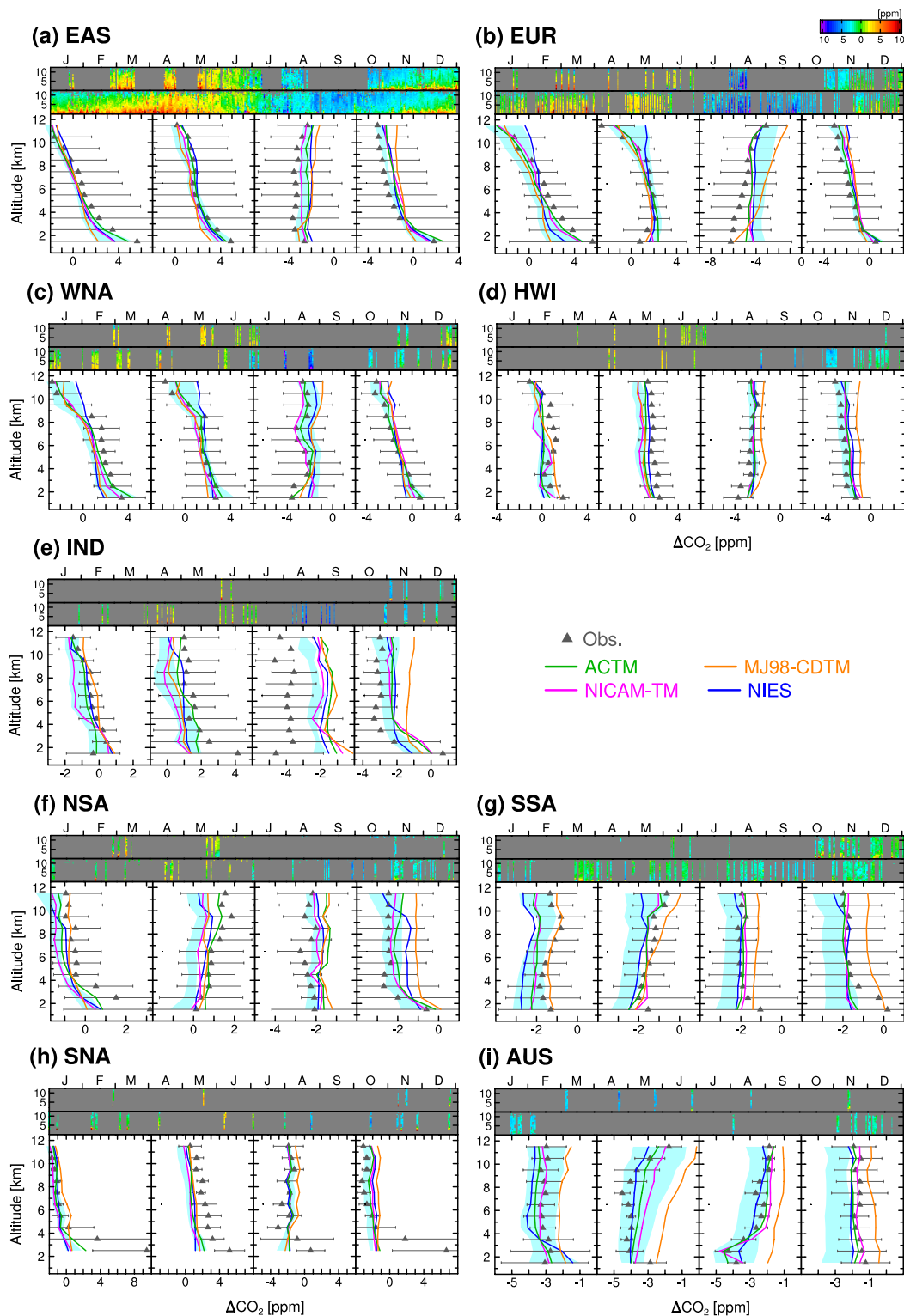


Fig. 5. Seasonal mean vertical profiles of CO₂ over each designated area for 2006–2007. Lines are simulated results using Flux2: ACTM (green), MJ98-CDTM (orange), NICAM-TM (magenta) and NIES (blue). Cyan shading shows the range of the simulated results obtained using Flux1. Gray triangles show the values corresponding to the CONTRAIL measurements. The error bar indicates the variation of the instantaneous data, derived by averaging the standard deviations of the instantaneous data within each grid at each level. Vertical profiles are seasonally averaged for January–February–March (JFM), April–May–June (AMJ), July–August–September (JAS), and October–November–December (OND). The top two panels (with gray background) in each figure show time–altitude cross-section of daily ΔCO_2 from the CONTRAIL data for 2006 (upper panel) and 2007 (lower panel).

3.2.1 Northern areas (EAS, EUR, WNA, HWI)

Over northern areas on the edge of landmass (EAS, EUR, WNA), large vertical gradients up to about 4 ppm are observed between near surface and FT. Then they seasonally vary in a wide range (Fig. 5a–c). Furthermore, during boreal winter-spring (JFM and AMJ), the CONTRAIL measurements show large vertical gradients (ca. 4 ppm) in the UT/LS region. Meanwhile, in HWI, much smaller gradients (ca. 2 ppm) are observed from near the surface to the upper troposphere throughout the year (Fig. 5d). Those vertical profile patterns are almost reproduced by the models (the average correlation coefficients are 0.92 and 0.94, respectively, for Flux1 and Flux2).

During boreal summer, differences between Flux1 and Flux2 are considerably large in northern terrestrial areas (during JAS, Flux2 has 1.9 Pg C yr⁻¹ larger uptake than Flux1). This flux difference caused significant changes of the vertical profiles for JAS. Especially in EUR and WNA, Flux2 consistently improved the model-observation agreement. Root mean square differences (RMSD) are lower by 0.4 and 0.2 ppm, respectively, for EUR and WNA.

Most simulated vertical gradients from PBL to FT are smaller than the observed ones for JAS, except EAS. One probable cause is a deficiency of the model vertical mixing. Actually, Stephens et al. (2007) reported that the TransCom3 models have overly strong vertical mixing from PBL to FT during boreal summer. In this comparison, however, weakening vertical mixing might not improve the results because ΔCO_2 simulated by MJ98-CDTM, which has the weakest vertical mixing as shown in Fig. 4, is more largely different from the observed one in the FT. Therefore, although the possibility of transport processes other than vertical mixing causing the model-observation discrepancies cannot be ruled out, we consider that flux uncertainty is significant to the simulated PBL-FT gradients. It is because the PBL-FT gradients were changed greatly by selection of the surface flux for JAS. To investigate transport uncertainties further, we should compare the simulated radon results with vertical radon observations (if available) but this is left for the future work.

3.2.2 Indian subcontinent (IND)

Over the Indian subcontinent (IND), model-observation mismatches of the vertical profiles are larger than those of the northern profiles (the averaged RMSD by Flux2 is 1.28 ppm for all seasons) (Fig. 5e). Especially, in JAS, the models overestimated ΔCO_2 at all levels and failed to reproduce the large vertical gradient near the surface (the averaged RMSD by Flux2 is 2.41 ppm). During boreal summer, a strong anticyclone circulation confines surface flux signals over the Indian continent preventing from mixing with surrounding air masses in the upper troposphere. Therefore the observed CO₂ concentrations up to the upper troposphere predomi-

nantly represent the surface flux on the Indian continent (Patra et al., 2011). Furthermore, despite the large range of cumulus convection schemes in the models, all the models consistently overestimated ΔCO_2 . Those facts suggest the need to put stronger sinks in that area of the flux data. Vigorous vertical transport within the Indian summer monsoon circulation rapidly ventilated low CO₂ air from near the surface to the upper troposphere, which the models were unable to reproduce because of insufficient sinks. It engenders a noticeable model-observation mismatch in FT. Actually, we confirmed a strong impact of surface flux on the simulated vertical profiles. The models with Flux1 simulated the vertical profiles closer to the observed one (the averaged RMSD = 1.69 ppm), although it is still insufficient. In fact, the time-integrated amount of Flux1 in IND for JAS (-3.12 g C m^{-2}) is much smaller than that of Flux2 (9.32 g C m^{-2}). The large model-observation mismatch is attributable to the fact that flux inhomogeneity in the Indian region is not constrained in Flux2 because the inversion of Flux2 had a large flux estimate region there that includes East Asia, South Asia, and Central Asia. A more detailed inversion study by Patra et al. (2011) estimated a large CO₂ uptake of about 1.8 Pg C yr⁻¹ during the summer in South Asia using ACTM as a forward transport model, GLOBALVIEW-CO₂ data product and flask measurements of CARIBIC (Schuck et al., 2010), and was subsequently validated by comparison with CONTRAIL data over Delhi and in the upper troposphere. Here, we used four different models to confirm the requirement of the strong sink.

Results also show pronounced model-observation mismatches (RMSD by Flux2 is 1.11 ppm) for AMJ. The CONTRAIL measurement shows high CO₂ near the surface and a consequently large PBL-FT gradient. However the models failed to reproduce it. Those mismatches are especially prominent in April (not shown). Over the Indian subcontinent, the period of April corresponds to the end of the dry season. The air temperature is quite high during the period. Therefore, that model underestimation might result from further sources from terrestrial biosphere respirations or biomass burnings (Patra et al., 2011).

3.2.3 Southeast Asia (NSA, SSA)

Features of the vertical profile over Southeast Asia differ greatly from those in northern areas (Figs. 5f and 5g). Both over NSA and SSA, CO₂ concentrations in the upper troposphere are about 1–2 ppm higher than those near the surface for AMJ. During this season, net non-fossil CO₂ flux in Southeast Asia and western Pacific is not a strong sink but a rather weak source (0.50, 0.77 Pg C yr⁻¹ respectively for Flux1 and Flux2). Therefore, the feature of CO₂ concentration increasing with height is probably induced by surface CO₂ signals from other areas that were transported through the upper troposphere. The models generally captured that feature.

Over SSA, the average ΔCO_2 simulated from Flux2 is 0.7 ppm larger throughout a year and 0.37 ppm closer to the observed one than that from Flux1. The Flux1-Flux2 difference of the annual net flux in Southeast Asia and western Pacific is small (0.06, $-0.04 \text{ Pg C yr}^{-1}$ respectively for Flux1 and Flux2). Therefore, the improvement of the model-observation mismatch by Flux2 is attributed to other large-scale flux patterns. Probably, it is induced by strong annual net sources in other terrestrial tropical areas of Flux2 (see Table 1).

It should also be noted that all the models failed to reproduce steep vertical gradients of 1–2 ppm near the surface over SSA persisting in all seasons. This failure is mostly attributable to the representation error of fossil-fuel emission. One possible cause is that a large amount of fossil fuel emissions on a small island, such as Jakarta on Java Island, is not well represented in the model grids. A test simulation by ACTM using recently updated fossil fuel emission data (EDGAR-4, 2009), in which a strong source marginally exists on Java Island, we produced a closer vertical gradient to the observed one (not shown). The representation error of the fossil fuel emission might exist in other places, but we could not find such kind of errors so clearly in the global models. We here show the error over Jakarta as a typical case.

3.2.4 Southern North America (SNA)

Over SNA, results show apparent model-observation mismatches of vertical gradients at lower altitudes, which are much larger than the model-model differences (Fig. 5h). In the area, JAL airplanes arrive and depart at the airport in Mexico City, which is located in a basin surrounded by high mountains. This topography strongly traps polluted air near the surface. However, in the global models, the topography is smoothed out and such phenomena are not well represented.

3.2.5 Australia (AUS)

Over AUS, atmospheric CO₂ largely varies not only at lower altitudes but also in the UT/LS region (Fig. 5i). The feature of high CO₂ in the upper troposphere during AMJ is similar to those over Southeast Asia, which suggests that high-CO₂ air from the Northern Hemisphere intruded into the Southern Hemisphere through the tropical upper troposphere. This transport mechanism has already been indicated from air sampling measurements of commercial airlines between Japan and Australia conducted by Nakazawa et al. (1991) and Matsueda et al. (2002), which are a predecessor and a part of the current CONTRAIL project. Furthermore, the theoretical framework of the inter-hemispheric transport of CO₂ is explained by Miyazaki et al. (2008) using ACTM simulation. For this study, we confirmed that mechanism from the vertical profiles. For AMJ, the models show the same increasing profiles as the observed one, but model-model differences are quite large. Those differences are in-

duced by differences of the inter-hemispheric exchange rate among the models. For all the seasons, the highest mean ΔCO_2 is simulated by MJ98-CDTM, which has the fastest inter-hemispheric exchange, whereas the lowest mean ΔCO_2 is simulated by NIES, which has the slowest one (Fig. 2).

3.3 Seasonal variations

Figure 6 portrays monthly mean variations of the simulated and observed CO₂ at 5–6 km over each area using data for 2006–2007. Each seasonal variation is derived from the binned ΔCO_2 data. Over all the nine areas, the models reasonably reproduced seasonal variations both with Flux1 and Flux2 (Table 5). Over most areas, seasonal amplitudes simulated from Flux2 are larger and closer to the observed one than those from Flux1 (Table 5). However, most of those changes are still not significant at 95 % confidence level, i.e., model-model differences are large compared to the changes by the fluxes. Furthermore, the seasonal amplitudes simulated from Flux2 are still smaller than the observed one over all the areas.

3.3.1 North

For comparison of CO₂ seasonal variations from at surface background sites in MBL to the upper troposphere, we averaged seasonal variations of the simulated and observed CO₂ at 4–5 km and 7–8 km in FT and in MBL of the northern area (Fig. 7). CONTRAIL has fewer measurement gaps during 2007 (see each upper panel in Fig. 5). Therefore, we used only data for 2007 here. The seasonal variation in FT is derived by averaging seasonal variations over three northern areas (EAS, EUR, and WNA). For MBL, we averaged seasonal variations from CO₂ records at 6 MBL sites located between 20° N and 70° N, which are also detrended by the linear trend at Minamitorishima.

Using northern CO₂ vertical profiles, Yang et al. (2007) calculated amplitude ratios of seasonal variations at upper and lower levels, and suggested that the TransCom3 models underestimated vertical propagation speed of seasonal variation in FT. We calculated similar amplitude ratios using the amplitude at 4–5 km as the reference. The seasonal amplitude ratios at 7–8 km simulated by ACTM, NICAM-TM, and NIES (0.81–0.89) are comparable to the observed one (0.86), irrespective of flux data used (Table 6). It indicates that those models reasonably simulated the vertical propagation of seasonal CO₂ variation within FT, differently from the TransCom3 models. Compared to those models, MJ98-CDTM shows quite a small amplitude ratio (0.69, 0.73 for Flux1, Flux2). This underestimation by MJ98-CDTM is related to the slower vertical transport inferred from the lower radon concentration in the upper troposphere compared to the other three models (Fig. 3).

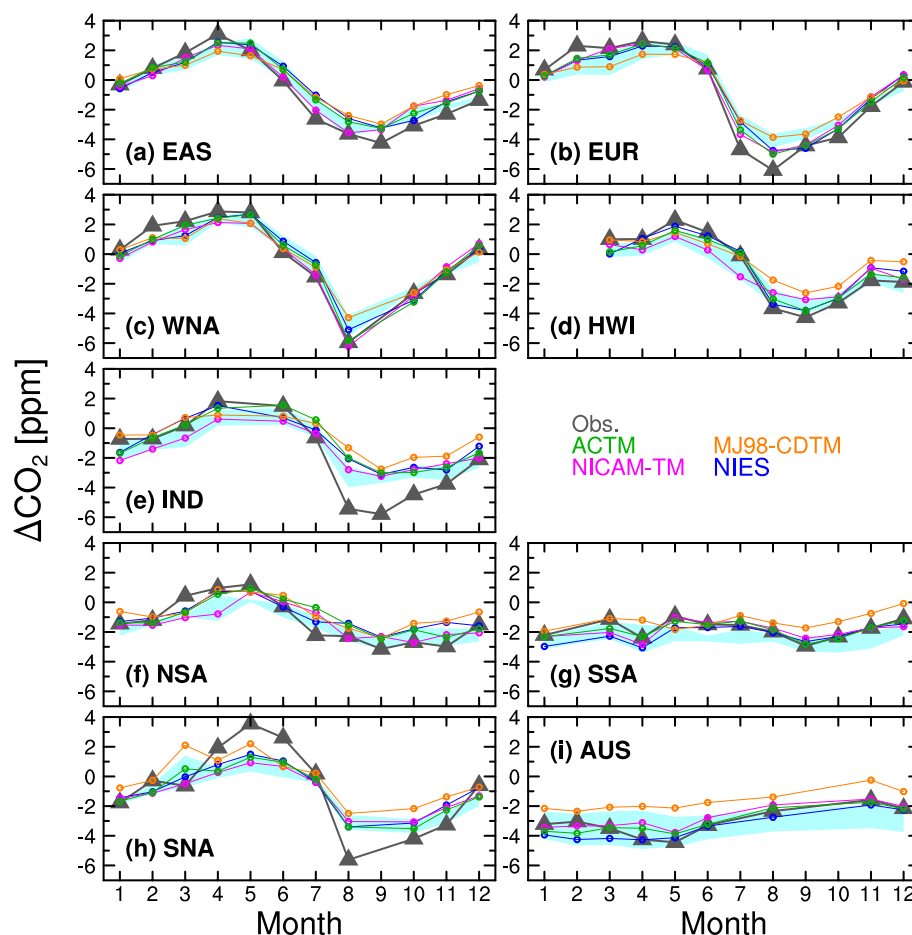


Fig. 6. Monthly mean variations of ΔCO_2 at 5–6 km over each area for 2006–2007. Gray triangles with lines show the values for the CONTRAIL measurements. Circles with lines are for simulated results from Flux2: ACTM (green), MJ98-CDTM (orange), NICAM-TM (magenta), and NIES (blue). Cyan shade shows range of the simulated results from Flux1.

Meanwhile, the model-model difference of amplitude ratio in MBL are rather large (1.26–1.69), indicating large model uncertainty for vertical transport from the near surface to FT. Furthermore, flux uncertainty should also be noted, as indicated by significant changes of the amplitude ratio by the fluxes (15–30%). These ratio changes according to the fluxes also indicate that the CONTRAIL measurements in FT caught different signals of surface CO₂ flux from those caught by the MBL sites. Probably, that is true because CONTRAIL measurements are affected by terrestrial fluxes more strongly than the MBL ones are, justifiably because of their continental locations. In contrast, the amplitude ratios at 7–8 km are not so affected by the fluxes. This small impact of the fluxes indicates that seasonal flux signals are almost identical at 4–5 km and 7–8 km.

3.3.2 Tropics

Figure 8 shows the same seasonal variations as those shown in Fig. 7, but for two tropical areas. The seasonal variations

in FT are derived respectively from the binned ΔCO_2 data over the Southeast areas of NSA and SSA. The MBL seasonal variations are derived respectively from CO₂ records at Guam and Christmas Island, which are located latitudinally near each Southeast Asian area.

Over NSA, the seasonal amplitude at 4–5 km is about 1 ppm smaller than that at each MBL site, although the seasonal amplitude at 7–8 km is larger (Fig. 8). Seasonal amplitudes in FT over SSA are a half to a third of those over NSA; furthermore, they have two minima, whereas the MBL one has one minimum. The models simulated most of those features (the average correlations are more than 0.7). However, the models consistently underestimated seasonal amplitudes, as they do in the northern area. Especially, the model-observation mismatches at the seasonal maximum and minimum are notable at 7–8 km. This is probably because the seasonal CO₂ variation in the Northern Hemisphere, whose amplitude is underestimated by the models, intruded towards the south via the tropical upper-troposphere.

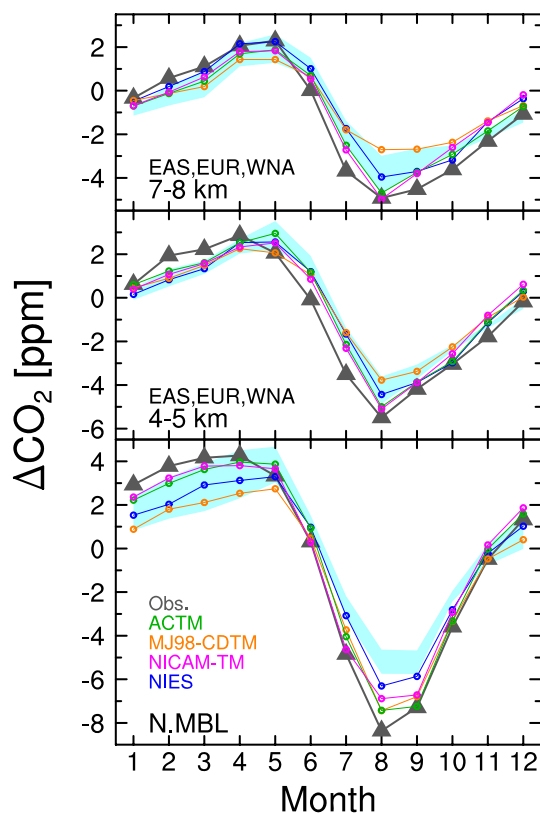


Fig. 7. Monthly mean variations of ΔCO_2 in the northern area for 2007. Data are averages of seasonal variations at six marine boundary layer (MBL) sites located between 20°N and 70°N for N, MBL (bottom panel) and at 4–5 km (middle panel) and 7–8 km (top panel) over the northern area, as aggregated from East Asia (EAS), Europe (EUR) and western North America (WNA). Gray triangles with lines show the results derived from CONTRAIL/GLOBALVIEW-CO₂. Circles with lines are simulated results from Flux2: ACTM (green), MJ98-CDTM (orange), NICAM-TM (magenta), and NIES (blue). Cyan shade shows range of the simulated results from Flux1.

3.4 Latitudinal profiles

Figure 9 shows the latitudinal mean profile of ΔCO_2 at 5–6 km in FT and in MBL for JFM and JAS of 2007. During JFM, both at 5–6 km and in MBL, the observed latitudinal profile is in the range of the model uncertainty. At 5–6 km, the simulated profile is apparently affected by the inter-hemispheric exchange rate; MJ98-CDTM, which has the fastest inter-hemispheric exchange rate, showed the smallest simulated inter-hemispheric gradient (2.3 ppm), whereas NIES, which has the slowest inter-hemispheric exchange rate, showed the largest simulated inter-hemispheric gradient (3.4 ppm). Meanwhile, in MBL, the simulated profiles are in a much wider range (2.4–4.3 ppm). Probably the simulated profile is affected not only by inter-hemispheric exchange but also by vertical mixing near the surface. This model-model difference is apparently greater than differences by

Table 5. Seasonal amplitudes of the observed and simulated concentrations at 5–6 km over each area for the period 2006–2007, and correlation coefficients between the observed and simulated seasonal cycles. The simulated amplitudes are averaged for the four models. Bold font in the Flux2 column represents a value significantly different from Flux1 at 95 % confidence level. The average correlation coefficient is derived by back transforming the averaged Fisher z . All the correlations are significant at 95 % confidence level.

Region	Seasonal amplitude			Correlation coefficient	
	Obs.	Flux1	Flux2	Flux1	Flux2
EAS	7.34	5.65	5.59	0.97	0.98
EUR	8.71	6.48	6.85	0.97	0.99
WNA	8.83	7.25	7.83	0.97	0.98
HWI	6.55	4.83	4.86	0.98	0.98
IND	7.61	4.42	4.17	0.95	0.93
NSA	4.36	3.19	3.28	0.87	0.87
SSA	2.01	1.37	1.71	0.78	0.75
SNA	9.17	4.72	4.60	0.94	0.96
AUS	2.86	1.36	2.21	0.85	0.86

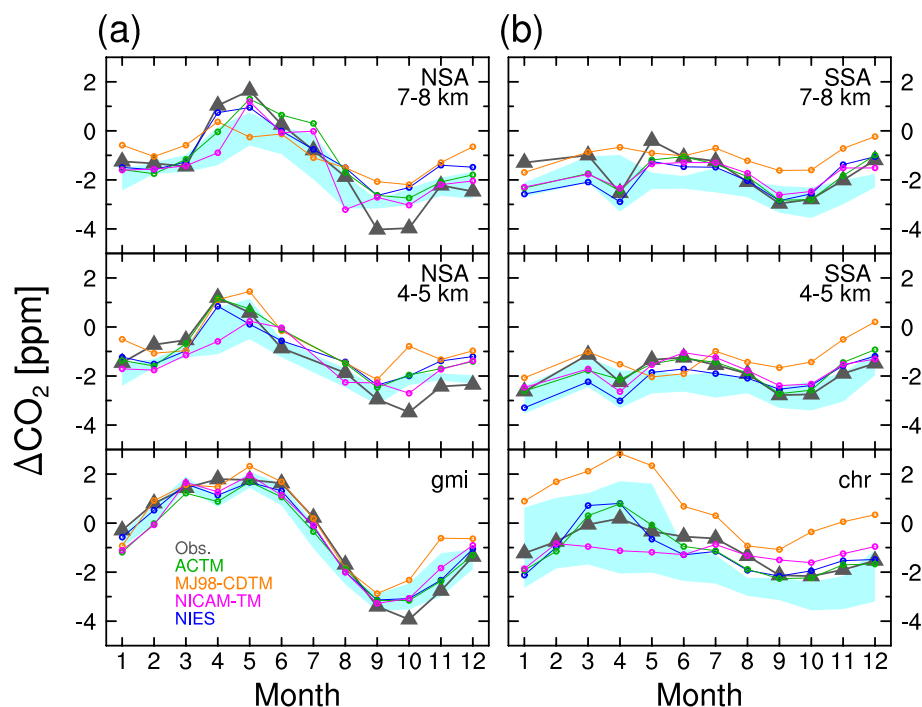
the fluxes, indicating that the transport model uncertainty is predominant to the latitudinal profile in MBL during boreal winter.

In contrast, during JAS, the results are quite sensitive to the flux data. Despite comparable north-tropics difference of carbon budgets between Flux1 and Flux2 to that for JFM (ca. 4Pg C yr^{-1} , see Table 1), the simulated latitudinal gradients are considerably changed by the fluxes. At 5–6 km, the north-tropics mean gradients (north: 20°S – 20°N , tropics: 20°S – 20°N) simulated from Flux2 are 0.5–0.8 ppm larger than those from Flux1 (Table 7a) and those differences are comparable to or greater than model-model differences, which suggests that active summer vertical transport ventilates some significant flux signals up to FT and those could be captured by the models.

However, we found apparent discrepancies between the observed and simulated north-tropics mean gradients. At 5–6 km and in MBL, the gradients of 4.7 and 1.8 ppm are observed, respectively. All the models with Flux2 underestimated those by 0.3–2.0 and 0.5–1.1 ppm (mean CO₂ in tropics is larger than that in north). The smaller simulated north-tropics gradient indicates requirements of stronger net carbon sink in the northern area and/or stronger net source in the tropics in the flux data. Here, we infer the stronger terrestrial net sink in the northern area during boreal summer. At the MBL sites for 2007, the observed growth rate is 0.8ppm yr^{-1} smaller than the simulated one from Flux2, on average. That discrepancy is 0.5ppm yr^{-1} larger in the northern area than that in the tropical area. These facts indicate further sinks in the northern area during boreal summer. The possibility of a stronger net source in the tropics during boreal summer is ruled out because the tropics-south mean

Table 6. Ratios of seasonal amplitudes to that at 4–5 km in the northern area for 2007. Simulated results are derived using Flux2 and Flux1 (parenthetical values).

	Obs.	ACTM	MJ98-CDTM	NICAM-TM	NIES
N. MBL	1.51	1.43 (1.31)	1.69 (1.47)	1.40 (1.27)	1.37 (1.26)
EAS, EUR, WNA (7–8 km)	0.86	0.83 (0.81)	0.69 (0.73)	0.89 (0.88)	0.89 (0.89)

**Fig. 8.** Monthly mean variations of ΔCO_2 over the Southeast Asia areas (NSA and SSA) at two altitude ranges (top two panels), and at two MBL sites in NSA and SSA latitude bands (gmi, chr) for 2007. Gray triangles with lines show data derived from CONTRAIL/GLOBALVIEW. The symbol/line and shaded area convention are same as Fig. 7.

gradient of CO₂ is well simulated by the models. Moreover, compared to that in MBL, the models largely underestimated the north-tropics mean gradient observed by CONTRAIL in FT. Using Flux2, the degrees of the model underestimation of the north-tropics mean gradient in FT are 10–44% larger than those in MBL. The CONTRAIL data in FT are more likely to be affected by terrestrial fluxes, as discussed in the previous section. Therefore, it is suggested that most of the further sinks should exist in northern terrestrial areas. One prominent candidate of those sinks is the strong uptake in IND (20–30° N) that was inferred from the vertical profile comparison (Sect. 3.2.2).

4 Conclusions

We elucidated three-dimensional structures of atmospheric CO₂ extensively using globally located vertical profile measurements of CONTRAIL and surface measurements of GLOBALVIEW. We investigated model performances in reproducing the three-dimensional CO₂ structures and their variations. Furthermore, using four independent transport models and two different fluxes, we evaluated the relative contributions of model and flux uncertainties. Furthermore, some implications for regional carbon budgets were obtained by comparing the simulations and the observations.

In general, the models reproduced the spatiotemporal patterns of CO₂ concentrations observed by CONTRAIL. Seasonal mean vertical profiles and vertical propagation of seasonal variation in the FT are mostly well simulated by the models. Furthermore, we confirmed reasonable model

Table 7. Latitudinal difference of mean ΔCO_2 between north (20–70° N) and tropics (20° S–20° N) at 5–6 km in the free-troposphere (a) and in the marine boundary layer (MBL) (b). Simulated results are derived using Flux2 and Flux1 (parenthetical values).

(a) 5–6 km					
	OBS	ACTM	MJ98-CDTM	NICAM-TM	NIES
JFM	1.90	2.15 (2.15)	1.29 (1.18)	2.20 (2.10)	2.21 (2.26)
JAS	−1.83	−1.14 (−0.30)	−0.83 (−0.24)	−1.37 (−0.83)	−0.75 (0.01)
(b) MBL					
	OBS	ACTM	MJ98-CDTM	NICAM-TM	NIES
JFM	3.88	3.73 (4.10)	1.21 (1.12)	3.89 (4.13)	2.83 (3.07)
JAS	−4.70	−3.72 (−1.85)	−4.19 (−2.26)	−3.98 (−1.76)	−2.66 (−1.09)

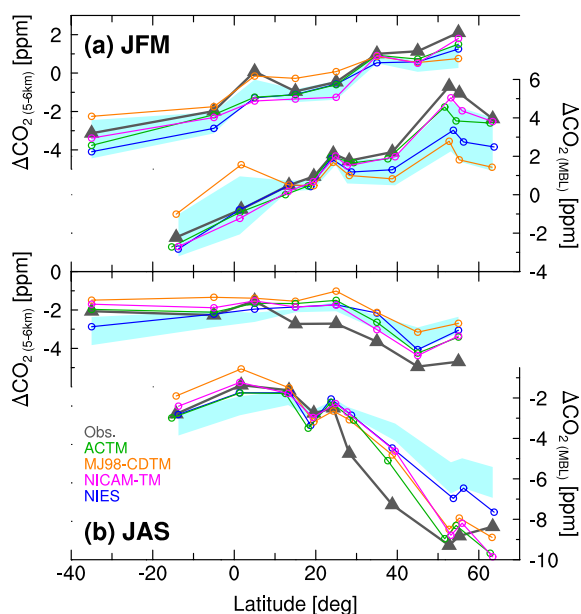


Fig. 9. Latitudinal mean profile of ΔCO_2 at 5–6 km in the free-troposphere (upper) and at the marine boundary layer (MBL) sites (lower) for January-February-March (JFM) (a) and July-August-September (JAS) (b) of 2007. Gray triangles with lines show the observed data from CONTRAIL. The symbol/line and shaded area convention are same as Fig. 7.

performance for reproducing CO₂ variations even over Southeast Asia, where measurements have not been conducted sufficiently to date. The CONTRAIL measurements suggested that northern CO₂ intruded southward through the upper troposphere. We confirmed that the models simulated that feature overall.

However, results show marked discrepancies between the observations and simulations. Especially, the discrepancy over the Indian continent during July-August-September is noteworthy; it indicates quite a strong carbon sink in that area, which has been unconstrained by the prior inversion.

From comparison of latitudinal gradients in FT and MBL, we found that the differences by the fluxes are comparable to or greater than model-model differences in summer. It suggests that active summer vertical transport ventilates some significant flux signals up to FT and those could be captured by the models. On the other hand, the model-model difference is much greater than the differences by the fluxes, suggesting that the transport model uncertainty is predominant during boreal winter.

Acknowledgements. We are grateful to the many engineers of Japan Airlines, JAMCO Tokyo for operating the measurement system. We would like to acknowledge JAL Foundation for coordinating the CONTRAIL project. We also thank the anonymous reviewers for their valuable comments on this manuscript. The CONTRAIL project is financially supported by the Research Fund by Global Environmental Research Coordination System of the Ministry of the Environment (MOE) in Japan. Our appreciation is also extended to the many research groups contributing to the GLOBALVIEW-CO₂ data product. The datasets used for this study were provided by the cooperative research project of the JRA-25/JCDAS long-term reanalysis by Japan Meteorological Agency (JMA) and Central Research Institute of Electric Power Industry (CRIEPI). YN thanks Hirofumi Tomita and other members at Research Institute for Global Change/JAMSTEC and at The University of Tokyo for developing NICAM.

Edited by: M. Heimann

References

- Arakawa, A. and Schubert, W.: Introduction of cumulus cloud ensemble with the large-scale environment. Part I, *J. Atmos. Sci.*, 31, 671–701, 1974.
- Baker, D. F., Law, R. M., Gurney, K. R., Rayner, P., Peylin, P., Denning, A. S., Bousquet, P., Bruhwiler, L., Chen, Y.-H., Ciais, P., Fung, I. Y., Heimann, M., John, J., Maki, T., Maksyutov, S., Masarie, K., Prather, M., Pak, B., Taguchi, S., and Zhu, Z.: TransCom 3 inversion intercomparison: Impact of

- transport model errors on the interannual variability of regional CO₂ fluxes, 1988–2003, *Global Biogeochem. Cy.*, 20, GB1002, doi:10.1029/2004/GB002439, 2006.
- Belikov, D., Maksyutov, S., Miyasaka, T., Saeki, T., Zhuravlev, R., and Kiryushov, B.: Mass- conserving tracer transport modeling on a reduced latitude-longitude grid with NIES-TM, *Geosci. Model Dev.*, 4, 207–222, doi:10.5194/gmd-4-207-2011, 2011.
- Boden, T. A., Marland, G., and Andres, R. J.: Global, Regional, and National Fossil Fuel CO₂ Emissions, Carbon Dioxide Information Analysis Center, Oak Ridge National Laboratory, US Department of Energy, Oak Ridge, Tenn, USA, doi:10.3334/CDIAC/00001, 2009.
- Chevallier, F., Ciais, P., Conway, T. J., Aalto, T., Anderson, B. E., Bousquet, P., Brunke, E. G., Ciattaglia, L., Esaki, Y., Fröhlich, M., Gomez, A., Gomez-Pelaez, A. J., Haszpra, L., Krummel, P. B., Langenfelds, R. L., Leuenberger, M., Machida, T., Maignan, F., Matsueda, H., Morguí, J. A., Mukai, H., Nakazawa, T., Peylin, P., Ramonet, M., Rivier, L., Sawa, Y., Schmidt, M., Steele, L. P., Vay, S. A., Vermeulen, A. T., Wofsy, S., and Worthy, D.: CO₂ surface fluxes at grid point scale estimated from a global 21 year reanalysis of atmospheric measurements, *J. Geophys. Res.*, 115, D21307, doi:10.1029/2010JD013887, 2010.
- Crevoisier, C., Sweeney, C., Gloor, M., Sarmiento, J. L., and Tans, P. P.: Regional US carbon sinks from three-dimensional atmospheric CO₂ sampling, *Proc. Natl. Acad. Sci. USA*, 107, 18348–18353, 2010.
- Denning, A. S., Randall, D. A., Collatz, G. J., and Sellers, P. J.: Simulations of terrestrial carbon metabolism and atmospheric CO₂ in a general circulation model. Part 2: Spatial and temporal variations of atmospheric CO₂, *Tellus*, 48B, 543–567, 1996.
- Dentener, F., Feichter, J., and Jeuken, A.: Simulation of the transport of Rn²²² using on-line and off-line global models at different horizontal resolutions: a detailed comparison with measurements, *Tellus*, 51B, 573–602, 1999.
- EDGAR-4: European Commission, Joint Research Centre (JRC)/Netherlands Environmental Assessment Agency (PBL), Emission Database for Global Atmospheric Research (EDGAR), release version 4.0, <http://edgar.jrc.ec.europa.eu>, 2009.
- Geels, C., Gloor, M., Ciais, P., Bousquet, P., Peylin, P., Vermeulen, A. T., Dargaville, R., Aalto, T., Brandt, J., Christensen, J. H., Frohn, L. M., Haszpra, L., Karstens, U., Rödenbeck, C., Ramonet, M., Carboni, G., and Santaguída, R.: Comparing atmospheric transport models for future regional inversions over Europe – Part 1: mapping the atmospheric CO₂ signals, *Atmos. Chem. Phys.*, 7, 3461–3479, doi:10.5194/acp-7-3461-2007, 2007.
- Gerbig, C., Lin, J. C., Wofsy, S. C., Daube, B. C., Andrews, A. E., Stephens, B. B., Bakwin, P. S., and Grainger, C. A.: Toward constraining regional-scale fluxes of CO₂ with atmospheric observations over a continent: 1. Observed spatial variability from airborne platforms, *J. Geophys. Res.*, 108, 4756, doi:10.1029/2002JD003018, 2003.
- GLOBALVIEW-CO₂: Cooperative Atmospheric Data Integration Project–Carbon Dioxide CD-ROM, NOAA CMDL, Boulder, Colorado, also available online via anonymous FTP to <ftp.cmdl.noaa.gov>, Path: [ccg/co2/GLOBALVIEW](ftp://ftp.cmdl.noaa.gov/ccg/co2/GLOBALVIEW), 2010.
- Grell, G. A.: Prognostic evaluation of assumptions used by cumulus parameterizations, *Mon. Weather Rev.*, 121, 764–787, 1993.
- Gurney, K. R., Law, R. M., Denning, A. S., Rayner, P. J., Pak, B. C., Baker, D., Bousquet, P., Bruhwiler, L., Chen, Y.-H., Ciais, P., Fung, I. Y., Heimann, M., John, J., Maki, T., Maksyutov, S., Peylin, P., Prather, M., and Taguchi, S.: Transcom 3 inversion intercomparison: Model mean results for the estimation of seasonal carbon sources and sinks, *Global Biogeochem. Cy.*, 18, GB1010, doi:10.1029/2003GB002111, 2004.
- Jacob, D. J., Prather, M. J., Rasch, P. J., Shia, R.-L., Balkanski, Y. J., Beagley, S. R., Bergmann, D. J., Blackshear, W. T., Brown, M., Chiba, M., Chipperfield, M. P., Grandpré, J. D., Dignon, J. E., Feichter, J., Genthon, C., Grose, W. L., Kashibhatla, P. S., Köhler, I., Kritz, M. A., Law, K., Penner, J. E., Ramonet, M., Reeves, C. E., Rotman, D. A., Stockwell, D. Z., Velthoven, P. F. J. V., Verver, G., Wild, O., Yang, H., and Zimmermann, P.: Evaluation and intercomparison of global atmospheric transport models using ²²²Rn and other short-lived tracers, *J. Geophys. Res.*, 102, 5953–5970, 1997.
- Kanamitsu, M., Ebisuzaki, W., Woolen, J., Potter, J., and Fiorino, M.: NCEP/DOE AMPI-II Reanalysis (R-2), *B. Am. Meteorol. Soc.*, 83, 1631–1643, 2002.
- Kuo, H. L.: Further studies of the parameterization of the influence of cumulus convection on large scale flow, *J. Atmos. Sci.*, 31, 1232–1240, 1974.
- Law, R. M., Peters, W., Rödenbeck, C., Aulagnier, C., Baker, I., Bergmann, D. J., Bousquet, P., Brandt, J., Bruhwiler, L., Cameron-Smith, P. J., Christensen, J. H., Delage, F., Denning, A. S., Fan, S., Geels, C., Houweling, S., Imasu, R., Karstens, U., Kawa, S. R., Kleist, J., Krol, M. C., Lin, S.-J., Lokupitiya, R., Maki, T., Maksyutov, S., Niwa, Y., Onishi, R., Parazoo, N., Patra, P. K., Pieterse, G., Rivier, L., Satoh, M., Serrar, S., Taguchi, S., Takigawa, M., Vautard, R., Vermeulen, A. T., and Zhu, Z.: TransCom model simulations of hourly atmospheric CO₂: Experimental overview and diurnal cycle results for 2002, *Global Biogeochem. Cy.*, 22, GB3009, doi:10.1029/2007GB003050, 2008.
- Machida, T., Matsueda, H., Sawa, Y., Nakagawa, Y., Hirokuni, K., Kondo, N., Goto, K., Nakazawa, T., Ishikawa, K., and Ogawa, T.: Worldwide Measurements of Atmospheric CO₂ and Other Trace Gas Species Using Commercial Airlines, *J. Atmos. Ocean. Technol.*, 25, 1744–1754, 2008.
- Mahowald, N. M., Rasch, P. J., Eaton, B. E., Whittlestone, S., and Prinn, R. G.: Transport of ²²²radon to the remote troposphere using the Model of Atmospheric Transport and Chemistry and assimilated winds from ECMWF and the National Center for Environmental Prediction/NCAR, *J. Geophys. Res.*, 102, 28139–28151, 1997.
- Maki, T., Ikegami, M., Fujita, T., Yamada, K., Sawa, Y., Matsueda, H., Shibata, K., Niwa, Y., Patra, P. K., and Machida, T.: Development of on-line tracer transport model and validation of vertical tracer transport against aircraft data, 8th International Carbon Dioxide Conference, Jena, Germany, 13–19 September 2009, T4-014, 2009.
- Masarie, K. A. and Tans, P. P.: Extension and Integration of Atmospheric Carbon Dioxide Data into a Globally Consistent Measurement Record, *J. Geophys. Res.*, 100, 11593–11610, 1995.
- Matsueda, H., Inoue, H. Y., and Ishii, M.: Aircraft observation of carbon dioxide at 8–13 km altitude over the western Pacific from 1993 to 1999, *Tellus*, 54B, 1–21, 2002.
- Matsueda, H., Machida, T., Sawa, Y., Nakagawa, Y., Hirokuni, K., Ikeda, H., Kondo, N., and Goto, K.: Evaluation of atmospheric

- CO₂ measurements from new flask air sampling of JAL airliner observations, *Pap. Meteorol. Geophys.*, 59, 1–17, 2008.
- Mellor, G. L. and Yamada, T.: A Hierarchy of Turbulence Closure Models for Planetary Boundary Layers, *J. Atmos. Sci.*, 31, 1791–1806, 1974.
- Miura, H.: An upwind-biased conservative advection scheme for spherical hexagonal–pentagonal grids. *Mon. Weather Rev.*, 135, 4038–4044, 2007.
- Miyazaki, K., Patra, P. K., Takigawa, M., Iwasaki, T., and Nakazawa, T.: Global-scale transport of carbon dioxide in the troposphere, *J. Geophys. Res.*, 113, D15301, doi:10.1029/2007JD009557, 2008.
- Nakanishi, M. and Niino, H.: An improved Mellor–Yamada level 3 model with condensation physics: its design and verification, *Bound.-Layer Meteorol.*, 112, 1–31, 2004.
- Nakazawa, T., Miyashita, K., Aoki, S., and Tanaka, M.: Temporal and spatial variations of upper tropospheric and lower stratospheric carbon dioxide, *Tellus*, 43B, 106–117, 1991.
- Niwa, Y.: Numerical study on atmospheric transport and surface source/sink of carbon dioxide, Ph.D. thesis, Center for Climate System Research, The University of Tokyo, Japan, 178 pp., 2010.
- Niwa, Y., Tomita, H., Satoh, M., and Imasu, R.: A three-dimensional icosahedral grid advection scheme preserving monotonicity and consistency with continuity for atmospheric tracer transport, *J. Meteor. Soc. Jpn.*, 89, 255–268, 2011.
- Noda, A. T., Oouchi, K., Satoh, M., Tomita, H., Iga, S.-I., and Tsushima, Y.: Importance of the Subgrid-scale Turbulent Moist Process of the Turbulent Transport: on Cloud Distribution in Global Cloud-Resolving Simulations, *Atmos. Res.*, 96, 208–217, doi:10.1016/j.atmosres.2009.05.007, 2009.
- Olivier, J. G. J. and Berdowski, J. J. M.: Global emissions sources and sinks, A.A. Balkema Publishers/Swets & Zeitlinger Publishers, Lisse, The Netherlands, 2001.
- Olsen, S. C. and Randerson, J. T.: Differences between surface and column atmospheric CO₂ and implications for carbon cycle research, *J. Geophys. Res.*, 109, D02301, doi:10.1029/2003JD003968, 2004.
- Onogi, K., Tsutsui, J., Koide, H., Sakamoto, M., Kobayashi, S., Hatsushika, H., Matsumoto, T., Yamazaki, N., Kamahori, H., Takahashi, K., Kadokura, S., Wada, K., Kato, K., Oyama, R., Ose, T., Mannoji, N., and Taira, R.: The JRA-25 Reanalysis, *J. Meteor. Soc. Jpn.*, 85, 369–432, 2007.
- Patra, P. K., Law, R. M., Peters, W., Rödenbeck, C., Takigawa, M., Aulagnier, C., Baker, I., Bergmann, D. J., Bousquet, P., Brandt, J., Bruhwiler, L., Cameron-Smith, P. J., Christensen, J. H., Delage, F., Denning, A. S., Fan, S., Geels, C., Houweling, S., Imasu, R., Karstens, U., Kawa, S. R., Kleist, J., Krol, M. C., Lin, S.-J., Lokupitiya, R., Maki, T., Maksyutov, S., Niwa, Y., Onishi, R., Parazoo, N., Pieterse, G., Rivier, L., Satoh, M., Serar, S., Taguchi, S., Vautard, R., Vermeulen, A. T., and Zhu, Z.: TransCom model simulations of hourly atmospheric CO₂: Analysis of synoptic-scale variations of the period 2002–2003, *Global Biogeochem. Cy.*, 22, GB4013, doi:10.1029/2007GB003081, 2008.
- Patra, P. K., Takigawa, M., Dutton, G. S., Uhse, K., Ishijima, K., Lintner, B. R., Miyazaki, K., and Elkins, J. W.: Transport mechanisms for synoptic, seasonal and interannual SF₆ variations and “age” of air in troposphere, *Atmos. Chem. Phys.*, 9, 1209–1225, doi:10.5194/acp-9-1209-2009, 2009.
- Patra, P. K., Niwa, Y., Schuck, T. J., Brenninkmeijer, C. A. M., Machida, T., Matsueda, H., and Sawa, Y.: Carbon balance of South Asia constrained by passenger aircraft CO₂ measurements, *Atmos. Chem. Phys.*, 11, 4163–4175, doi:10.5194/acp-11-4163-2011, 2011.
- Pickett-Heaps, C. A., Rayner, P. J., Law, R. M., Ciais, P., Patra, P. K., Bousquet, P., Peylin, P., Maksyutov, S., Marshall, J., Rödenbeck, C., Langenfelds, R. L., Steele, L. P., Francey, R. J., Tans, P., and Sweeney, C.: Atmospheric CO₂ inversion validation using vertical profile measurements: Analysis of four independent inversion models, *J. Geophys. Res.*, 116, D12305, doi:10.1029/2010JD014887, 2011.
- Randerson, J. T., Thompson, M. V., Conway, T. J., Fung, I. Y., and Field, C. B.: The contribution of terrestrial sources and sinks to trends in the seasonal cycle of atmospheric carbon dioxide, *Global Biogeochem. Cy.*, 11, 535–560, 1997.
- Sarrat, C., Noihan, J., Lacarrère, P., Conier, S., Lac, C., Calvet, J. C., Dolman, A. J., Gerbig, C., Neininger, B., Ciais, P., Paris, J. D., Boumard, F., Ramonet, M., and Butet, A.: Atmospheric CO₂ modeling at the regional scale: Application to the CarboEurope Regional Experiment, *J. Geophys. Res.*, 112, D12105, doi:10.1029/2006JD008107, 2007.
- Satoh, M., Matsuno, T., Tomita, H., Miura, H., Nasuno, T., and Iga, S.: Nonhydrostatic icosahedral atmospheric model (NICAM) for global cloud resolving simulations, *J. Comput. Phys.*, 227, 3486–3514, 2008.
- Sawa, Y., Machida, T., and Matsueda, H.: Seasonal variations of CO₂ near the tropopause observed by commercial aircraft, *J. Geophys. Res.*, 113, D23301, doi:10.1029/2008JD010568, 2008.
- Schuck, T. J., Brenninkmeijer, C. A. M., Baker, A. K., Slemr, F., von Velthoven, P. F. J., and Zahn, A.: Greenhouse gas relationships in the Indian summer monsoon plume measured by the CARIBIC passenger aircraft, *Atmos. Chem. Phys.*, 10, 3965–3984, doi:10.5194/acp-10-3965-2010, 2010.
- Shibata, K., Yoshimura, H., Ohizumi, M., Hosaka, M., and Sugi, M.: A Simulation of Troposphere, Stratosphere and Mesosphere with an MRI/JMA98 GCM, *Pap. Meteorol. Geophys.*, 50, 15–53, 1999.
- Simmons, A., Uppala, S., Dee, D., and Kobayashi, S.: ERA-Interim: New ECMWF reanalysis products from 1989 onwards, *ECMWF, Newsletter No. 110 – Winter 2006/2007*, 25–35, 2007.
- Stephens, B. B., Gurney, K. R., Tans, P. P., Sweeney, C., Peters, W., Bruhwiler, L., Ciais, P., Ramonet, M., Bousquet, P., Nakazawa, T., Aoki, S., Machida, T., Inoue, G., Vinnichenko, N., Lloyd, J., Jordan, A., Heimann, M., Shibistova, O., Langenfelds, R. L., Steele, L. P., Francey, R. J., and Denning, A. S.: Weak Northern and Strong Tropical Land Carbon Uptake from Vertical Profiles of Atmospheric CO₂, *Science*, 316, 1732–1735, 2007.
- Takahashi, T., Sutherland, S. C., Wanninkhof, R., Sweeney, C., Feely, R. A., Chipman, D. W., Hales, B., Friederich, G., Chavez, F., Sabine, C., Watson, A., Bakker, D. C., Schuster, U., Metzl, N., Yoshikawa-Inoue, H., Ishii, M., Midorikawa, T., Nojiri, Y., Körtzinger, A., Steinhoff, T., Hoppema, M., Olafsson, J., Arnarson, T. S., Tilbrook, B., Johannessen, T., Olsen, A., Bellerby, R., Wong, C., Delille, B., Bates, N., and de Baar, H. J.: Climatological mean and decadal change in surface ocean pCO₂, and net sea-air CO₂ flux over the global oceans, *Deep-Sea Res., Part II*, 56, 554–577, 2009.

- Takigawa, M., Sudo, K., Akimoto, H., Kita, K., Takegawa, N., Kondo, Y., and Takahashi, M.: Estimation of the contribution of intercontinental transport during the PEACE campaign by using a global model, *J. Geophys. Res.*, 110, D21313, doi:10.1029/2005JD006226, 2005.
- Tiedtke, M.: A comprehensive mass flux scheme for cumulus parameterization in large-scale models, *Mon. Weather Rev.*, 117, 1779–1800, 1989.
- Tomita, H. and Satoh, M.: A new dynamical framework of nonhydrostatic global model using the icosahedral grid, *Fluid Dynam. Res.*, 34, 357–400, 2004.
- Xueref-Remy, I., Bousquet, P., Carouge, C., Rivier, L., and Ciais, P.: Variability and budget of CO₂ in Europe: analysis of the CAATER airborne campaigns – Part 2: Comparison of CO₂ vertical variability and fluxes between observations and a modeling framework, *Atmos. Chem. Phys.*, 11, 5673–5684, doi:10.5194/acp-11-5673-2011, 2011.
- Yang, Z., Washenfelder, R. A., Keppel-Aleks, G., Krakauer, N. Y., Randerson, J. T., Tans, P. P., Sweeney, C., and Wennberg, P. O.: New constraints on Northern Hemisphere growing season net flux, *Geophys. Res. Lett.*, 34, L12807, doi:10.1029/2007GL029742, 2007.